

Potent neutralization of Hepatitis A virus reveals a receptor mimic mechanism and the receptor recognition site

Xiangxi Wang^{1\$,*}, Ling Zhu^{2\$}, Minghao Dang^{1\$}, Zhongyu Hu^{3\$}, Qiang Gao^{1,4}, Shuai Yuan¹, Yao Sun¹, Bo Zhang⁴, Jingshan Ren², Abhay Kotecha², Thomas S Walter², Junzhi Wang³, Elizabeth E. Fry^{2*}, David I. Stuart^{2,6*} and Zihe Rao^{1,5*}

¹ National Laboratory of Macromolecules, Institute of Biophysics, Chinese Academy of Science, Beijing, 100101, China. ² Division of Structural Biology, University of Oxford, The Henry Wellcome Building for Genomic Medicine, Headington, Oxford OX3 7BN, UK. ³ National Institutes for Food and Drug Control, No. 2, TiantanXili, Beijing 100050, China. ⁴ Sinovac Biotech Co., Ltd., Beijing, 100085, China. ⁵ Laboratory of Structural Biology, School of Medicine, Tsinghua University, Beijing, 100084, China. ⁶ Diamond Light Sources, Harwell Science and Innovation Campus, Didcot OX11 0DE, UK.

^{\$} These authors contributed equally to this work.

* Correspondence should be addressed to DIS (Email: dave@strubi.ox.ac.uk), X.W. (Email: xiangxi@ibp.ac.cn), EEF (Email: liz@strubi.ox.ac.uk) or Z.R. (Email: raozh@xtal.tsinghua.edu.cn).

Abstract:

Hepatitis A virus (HAV) infects ~1.4 million people annually and whilst there is a vaccine, there are no licensed therapeutic drugs. HAV is unusually stable (making disinfection problematic) and little is known of how it enters cells and releases its RNA. Here we report a potent HAV-specific monoclonal antibody R10 that neutralizes HAV infection by blocking attachment to the host cell. High resolution cryo-EM structures of HAV full and empty particles and of the complex of HAV with R10 Fab reveal the atomic details of antibody binding and point to a receptor recognition site at the pentamer interface. These results, together with our observation that the R10 Fab destabilizes the capsid, suggest the use of a receptor mimic mechanism to neutralize virus infection, providing new opportunities for therapeutic intervention.

Key words: picornavirus, entry, neutralizing mechanism, receptor recognition

Significance Statement

Hepatitis A virus (HAV) remains enigmatic, being unusually stable physically. Where the receptor binds and how the virion can be destabilized to release the genome are unknown. We report a potent HAV-specific neutralizing monoclonal antibody R10 that blocks receptor attachment and interferes with viral uncoating. We have determined high resolution cryo-EM structures of HAV full particles, empty particles and full particles complexed with R10 Fab, revealing that R10 binds to the viral surface along the edges of the pentameric building block of the virus, and these interactions are critical for receptor binding and viral uncoating. Our results point to the use of a receptor mimic mechanism to neutralize virus infection highlighting new opportunities for therapeutic intervention.

\body

Introduction

HAV is an ancient and ubiquitous pathogen found in primates and small mammals (1). It is a picornavirus with many distinctive features: in the blood it is found in an enveloped form but is shed in feces as a naked, unenveloped particle (2); it possesses a low G/C ratio in the genome sequence and a strong codon bias (3); it grows poorly in tissue culture; it possesses a 67-residue carboxy-terminal extension of VP1 (VP1-2A or VPX), which is important for viral assembly (4) and has a very short, non-myristoylated VP4 (~23 residues) (5). Due to its unusual properties, HAV remains enigmatic and occupies an evolutionary position on the periphery of picornaviruses (6, 7).

Our previous crystal structure of unenveloped HAV(7) showed no trace of the canyon which encircles the 5-fold axes of enteroviruses and is often the site of receptor binding (8, 9). Indeed the structure provided no clues as to where T cell immunoglobulin and mucin 1 (TIM-1), the proposed receptor (10, 11), might attach. In addition the virus capsid contains no pocket factor and can withstand remarkably high temperature and low pH, indicating an uncoating mechanism (7) unlike that of enteroviruses; heating of HAV particles does not transform virions to an expanded state *in vitro*. Structural characterization of an HAV–TIM-1 complex might elucidate the cell entry mechanism, but difficulty in obtaining homogenous complex preparations due to the low binding affinity of TIM-1, at least for unenveloped

particles has made this challenging. However it is known that neutralizing antibodies (NABs) protect against virus infection by mechanisms that include blocking attachment to the cellular receptor, overstabilizing the virus, preventing viral genome release or physically destabilizing the virus (12, 13). Structural studies of virus complexes with such antibodies can therefore help illuminate these underlying biological functions. Here we identify a highly potent NAb R10 that can neutralize HAV infection efficiently by blocking attachment to the host cell. The complex structure of the HAV full particle and R10 Fab suggest where the receptor may bind, and together with the ability of the R10 Fab to destabilize the capsid, point to the use of a receptor mimic mechanism to neutralize virus infection.

Results

NAb R10 interferes with viral uncoating and prevents virus attachment

Twenty-five monoclonal antibodies were generated by immunizing mice. Of these, that named R10 had the strongest neutralizing activity against HAV (a 50% neutralizing concentration [neut₅₀] value of ~2nM, ~0.3 µg/ml). The Fab fragment is also strongly neutralizing (neut₅₀= ~3nM, ~0.45 µg/ml) (Fig. 1A). R10 does not recognize linear epitopes by immunoblot, but recognizes conformational epitopes by enzyme-linked immunosorbent assay (ELISA), and shows similar binding affinities to full and empty particles (Fig. 1B). Interestingly a fluorescent assay revealed that while the R10 Fab portion destabilizes full HAV particles by 7 °C, the intact R10

108 stabilizes the particles by 2 °C (Fig. 1C and Fig. S1A). The same assay indicates that
109 the bivalent intact antibody induces a two-stage transition in protein conformation to
110 release the RNA genome (Fig. 1C and Fig. S1A). The first event, producing a slight
111 exposure of RNA occurs at a similar temperature to that seen with the Fab, whereas
112 the second, which fully exposes the genome (Fig. 1C and Fig. S1B), occurs at a
113 slightly higher temperature than in the unliganded virus, presumably due to the two
114 arms of the antibody holding the particles together. TIM-1 IgV domain alone has no
115 effect on viral stability in thermofluor assays (Fig. S1C). This observation is
116 consistent with previous reports, which conclude that although TIM-1 IgV domain is
117 necessary for binding of HAV, both TIM-1 IgV domain and mucin domain are
118 required to trigger uncoating of HAV (14). Unlike FMDV, where uncoating is
119 initiated at low pH, HAV exhibits an extremely robust conformation at low pH (pH
120 5.0), even after R10 binding (Fig. S1C), suggesting acidic environment might not be
121 essential for HAV uncoating. Note that the HAV particles do not start to uncoat at
122 physiological temperatures even after destabilization by Fab. They continue to exist
123 as mature virions and remain stable as most picornaviruses, so that destabilization is
124 unlikely to be the neutralization mechanism. For HAV the mechanism of RNA
125 genome release remains unclear and it is possible that a cellular receptor or a specific
126 host factor may be required for particle disassembly. Given the ability of the R10
127 Fab to destabilize HAV, the binding sites on HAV of the host factor and R10 may
128 overlap partially or fully. To explore the mechanism of neutralization, real-time

reverse transcriptase-PCR (RT-PCR) was carried out to quantify the virus remaining on the cell surface, following exposure to antibodies pre- and post-virus attachment to cells at 4 °C. The results suggest that R10 prevents HAV attachment to the cell surface and is able to displace virus that has already bound to the cell receptor (Fig. 1D). In addition, R10 competitively blocked TIM-1 Ig V binding to HAV (Fig. S2A and S2B), consistent with R10 preventing HAV from attaching to host cells by blocking the binding of HAV to TIM-1.

Structure determination

Cryo-EM micrographs of the previously characterized (7) full and empty formaldehyde-inactivated HAV genotype TZ84 (HAV IA) particles and the R10 Fab:full particle complex were recorded using a FEI Polara electron microscope equipped with a Gatan K2 Summit detector (Fig. S3A-S3C). The structures of the HAV full particle, empty particle and the R10 Fab:full particle complex were determined at resolutions of 3.4, 3.8 and 4.2 Å with 4,587, 4,393 and 1,752 particles respectively by single-particle techniques using the “gold” standard FSC=0.143 criterion (15) (Fig. S3D-S3G). At 3.4 and 3.8 Å resolution, the cryo-EM electron density maps of the full and empty particles are well resolved for the most part, allowing us to place the X-ray structures (7) in the maps (Fig. S4) and then optimize and validate them using standard X-ray crystallographic derived methods (16) (Table S1). In addition the crystal structure of the isolated NAb Fab R10 was determined at

a resolution of 2.9 Å (Table S2). The 4.2 Å, cryo-EM map of the R10 Fab:full particle complex clearly reveals the polypeptide backbone, many bulky side chains and the mode of pathogen-antibody interaction (Fig. S4). To define precisely the atomic determinants of the interaction, the refined cryo-EM structure of the HAV full particle (3.4 Å) and crystal structure of the R10 Fab (2.9 Å) were fitted into the EM map and then refined against the phased structure factors calculated from the 4.2 Å EM map in Phenix (16).

Cryo-EM structures of HAV full particles and empty particles

The full and empty particles have indistinguishable external surfaces (Fig. 2A-2C), consistent with the similar binding affinities of R10 to the two types of particle (Fig. 1B). Major differences are seen in internal structures, many of which were previously seen when comparing the X-ray structures (7), including disordering of the N-terminal ~40 residues of VP1 and ~20 residues of VP0 around the 3-fold axes in the empty particle (Fig. 2E). However the EM map reveals clearer density for the RNA genome in the full particles, where it appears as multiple layers with visible contacts with the inner capsid (Fig. 2D). In piconaviruses, the single-stranded RNA genome is highly condensed and packed at $>800 \text{ mg ml}^{-1}$ (17), double the concentration for instance of the dsRNA *Reoviridae* (18), but the organization in piconaviruses has proved difficult to visualize. The layered structure we observe in HAV is slightly reminiscent of that observed in other virus families (18).

Structure of HAV full particles in complex with NAb R10 Fab

Understanding the structural basis of how R10 Fab prevents receptor(s) binding and destabilizes HAV (Fig. 1) may help resolve the enigma of how this virus, which is stable up to 80 °C and to extremes of pH, uncoats. The level of electron density for the Fab suggests that all or almost all of the possible 60 copies are attached to each virus particle (Fig. 3A and 3B). HAV capsid proteins exhibit no notable conformational changes upon binding to R10 Fab with an RMSD of 0.2 Å between the R10 Fab bound and unbound states of HAV. R10 binds to the viral surface along the edges of the pentameric building block of the virus, between the 2-fold and 3-fold axes in a similar position to that observed for AM28 antibody bound to parecho virus and NAb E18 binding to EV71 (13, 19) (Fig. 3C, 3D and Fig. S5). Specifically the Fab binds across the interface between pentamers, interacting with VP2 (interaction area 300 Å²) and VP3' from different pentamers (interaction area 753 Å²) (Fig. 3E and Fig. S6A and S6B). This epitope is only 18 Å from the nearest 2-fold axis and we note that in enteroviruses, the 2-fold axes separate during the initial stage of uncoating (20) so antibodies binding in this region might either prevent uncoating or catalyze premature uncoating. Indeed R10 Fab destabilizes HAV by 7 °C, although a temperature of over 60 °C is still required to trigger uncoating, so that whilst Fab binding will not trigger uncoating at physiological temperatures binding appears to favor a structure *en route* to uncoating. In contrast,

intact R10 slightly inhibits full uncoating, possibly by cross-linking pentamers,

The NAb R10 epitope

The heavy-chain and light-chain variable domains contribute ~60% and ~40% of the protein-protein interface respectively, with the heavy chain predominantly binding VP3, whilst the light chain binds VP2 and VP3 (Fig. S6A and S6B). The interaction surface on R10 comprises four of the six common complementary determining regions (CDRs): H1 (residue 28-32), H2 (residue 52-57), H3 (residue 100-106) and L1 (residue 30-31) with, unusually, additional interactions contributed by the light chain framework region (L1-2 residue 45-55) (Fig. 4A and Fig. S6A and S6B). The epitope on HAV includes residues 64-71 of VP2 and residues 68-78, 143-150, 209 and 246 of VP3 (Fig. 4A and Table S3). Residues comprising the epitope are 87.5% identical and 91.7% conserved across 6 human HAV genotypes (Fig. S6C and S6D), suggesting that R10 is likely to bind strongly to most human HAVs. Tight binding is facilitated by 19 hydrogen bonds, the antibody components of these include the side-chain of Y48 (L-chain), and main-chain carbonyl groups of V103 (H-chain) and L53 (L-chain) which interact with K150 (VP3) and R209 (VP3) respectively, and indirectly with R67 (VP2) (Fig. 4A).

NAb R10 may be a receptor mimic

Interestingly Fab binding displaces a string of sulphate ions bound to positive

213 charges, notably R67 of VP2, and K150 and R209 of VP3, which fringe the
214 pentameric assemblies (Fig. 4B) (7), an area predicted to bind the protein or glycans
215 of TIM-1. To test this we investigated whether sulphated glycans can inhibit HAV
216 infection and found that heparin significantly inhibited HAV infection in a
217 dose-dependent manner (Fig. 4C), consistent with TIM-1 facilitating cell entry by
218 attachment of its highly glycosylated mucin-like region to HAV in this region (14).
219 The extracellular portion of TIM-1 contains an N-terminal immunoglobulin
220 variable-like (Ig) domain (d1) followed by a mucin-like region. The Ig-like d1 is
221 required for binding of HAV, but without the mucin-like region soluble d1 binds and
222 neutralizes HAV inefficiently (14). d1 shares some structural similarity with both the
223 VH and VL domains of R10 Fab but is much more similar to the VL domain
224 (RMSDs for 89.3% and 95.4% of C α s are 5.3 Å and 3.4 Å for VH and VL
225 respectively) (Fig. S2C and S2D). Furthermore the major point of interaction of the
226 VH domain is in the extended CDR3 region, which has no structural similarity in d1,
227 the major interactions with the VL domain are with the framework region. Thus not
228 only is the VL domain similar to d1 of TIM-1, but it interacts with the virus via a
229 region which is not usually part of the antibody binding site, but can be part of the
230 adhesion surface in Ig-like adhesion molecules (21). It is therefore possible that
231 TIM-1 binding to HAV involves d1 attachment via interactions that recapitulate the
232 R10 VL contacts, with additional affinity conferred by interactions with the
233 mucin-like domain. The much weaker binding of TIM-1 than R10 is consistent with

much of the R10 affinity deriving from VH interactions, although assays of TIM-1 binding generally use *E. coli* expressed material lacking the mucin-like domain and so underestimate the strength of interaction. Nevertheless it is unlikely that attachment of a relatively small number of receptors could, alone, trigger uncoating of the very robust HAV particles.

Discussion

Uncoating – release of the viral genome into the host-cell cytosol, is key to picornavirus infection. Amongst picornaviruses, the process is best understood for enteroviruses, where uncoating is thought to proceed via expanded intermediate particles, which have been captured for structural analysis (20). In contrast aphtho- and cardioviruses appear to simply dissociate into pentamers (22), although an unidentified intermediate particle, facilitating directed egress of the RNA cannot be ruled out. In both cases the loss of interactions at the icosahedral 2-fold axes is a crucial step. Indeed these regions can be targeted to over-stabilize the virus capsid, for instance by capsid engineering for improved vaccines (23), or to destabilize the capsid, for example NAb E18 binds here and causes ejection of the genome from enterovirus EV71 (13). We have found that the potent NAb R10 Fab binds in this region and somewhat destabilizes the particles, consistent with HAV uncoating also proceeding via changes at the pentamer interface. Furthermore we find evidence that the TIM-1 receptor also binds in this region, perhaps using interactions resembling

those seen for the light chain of the R10 Fab. Neutralization is therefore presumably by preventing receptor binding. In summary our results demonstrate how increasing access to panels of authentic neutralizing monoclonal antibodies will facilitate structure-function studies to unpick the underlying biological processes of viral-host interactions, and will also provide new opportunities for therapeutic intervention.

Materials and Methods

Particle production and purification

HAV virus genotype TZ84 was propagated in 2BS cells at a multiplicity of infection (MOI) of 0.2 at 33-34 °C. Particle production and purification have been described previously (7).

Crystallization, data collection and structure determination

Purified Fab was concentrated to 8 mg/ml, and crystallization screening carried out using the sitting-drop vapour diffusion method in 96-well plates (24). Cubic crystals appeared in 20% PEG3350, 0.2 M Sodium Thiocyanate within 2 weeks. Cryo-cooling was carried out by soaking a crystal in reservoir solution containing 20% (v/v) glycerol and X-ray data were collected at I03, Diamond Light Source. Diffraction images (exposure time 0.1 s with 40% beam transmission) of 0.1° rotation were recorded on a PILATUS 6M detector, at a wavelength of 0.9765 Å to a

276 resolution of 2.9 Å.

277 Data were processed, integrated, and scaled using the HKL2000 package (25). The
278 crystal belongs to space group *P*21 with cell parameters $a = 52.5 \text{ Å}$, $b = 140.5 \text{ Å}$, $c =$
279 68.9 Å , $\alpha = 90^\circ$, $\beta = 110^\circ$, $\gamma = 90^\circ$. Structure determination by molecular replacement
280 with a Fab search model (PDB ID 1QGC (26)) used the program PHASER
281 (27). Manual model building and refinement were performed with COOT (28) and
282 PHENIX (29). Data collection and structure refinement statistics are given in Table
283 S2.

285 **Thermofluor assay**

286 Thermofluor experiments were performed with an MX3005p RT-PCR instrument
287 (Agilent). SYTO9 and SYPRO red (both Invitrogen) were used as fluorescent probes
288 to detect the presence of single-stranded RNA and exposed hydrophobic regions of
289 proteins, respectively (30-32). 50 µL reactions were set up in a thin-walled PCR
290 plate (Agilent), containing 1.0 µg of either virus or 1.0 µg of virus plus 3.0 µg of
291 R10 antibody (~120 R10 molecules per HAV virion) or 1.0 µg of virus plus 2.0 µg of
292 R10 Fab (~240 R10 Fab molecules per HAV virion) or 1.0 µg of virus plus 0.5 µg of
293 TIM-1 Ig V (~240 TIM-1 Ig V molecules per HAV virion), 5 µM SYTO9 and 3X
294 SYPRO red in PBS buffer solutions and ramped from 25-99 °C with fluorescence
295 recorded in triplicate at 1 °C intervals. The RNA release (Tr) and melting temperature
296 (Tm) were taken as the minima of the negative first derivative of the RNA exposure

and protein denaturation curves, respectively.

RT-PCR to quantitate virus on the cell surface

The amount of HAV remaining on the surface of 2BS cells after R10 treatment was estimated by quantitative RT-PCR as previously described(33). In brief, HAV was mixed with different concentrations of R10 before and after the virus attached to cells (MOI of ~ 1) at 4 °C. The cells were washed 3 times and total cellular RNA purified using RNeasy mini kit (Qiagen), as described in the manufacturer's instructions. Real-time quantitative PCR (qPCR) was performed using One Step SYBR PrimeScript™ RT-PCR Kit (TaKaRa) in a CFX 96 Real-Time System (Bio-rad). The 25µl reaction contained 12.5µl 2x One Step SYBR RT-PCR Buffer III, 0.5µl TaKaRa Ex Taq HS, 0.5µl PrimeScript RT Enzyme Mix II, 0.5µl each of 10µM forward (5'-TGG AAT CAC ATT AAA GCA AGC AA-3') and reverse primers (5'-GGA ACA CGA AAT CTC AAA GTT GAC T-3'), 2µl total RNA and 8.5µl RNase free H₂O. The thermal profile for qPCR was 42°C for 5min for reverse transcription, 95 °C for 10s for reverse transcription inactivation; this was followed by 40 cycles of denaturation at 95 °C for 10 s, annealing and extension at 60 °C for 30 s. GAPDH was used as the housekeeping gene to normalize samples (forward 5'-CTG TTG CTG TAG CCA AAT TCGT-3', reverse 5'-ACC CAC TCC TCC ACC TTT GAC-3'). The analysis of relative levels of HAV RNA in different samples was performed by comparative 2- $\Delta\Delta$ CT method (34).

318

319 **TIM-1 Ig V domain expression and purification**

320 Human TIM-1 Ig V domain (residues 22-129, d1) was cloned in a pET-22b vector
321 (Novagen) with a C-terminal 6×His-tag and expressed in *E. coli* BL21 (DE3). Soluble
322 receptor domain was prepared from inclusion bodies by in vitro refolding, purified
323 and activity checked as described previously (11).

324

325 **Cryo-EM and data collection**

326 Purified R10 Fab fragments were incubated with HAV full particles (at a
327 concentration of ~ 1 mg/ml) at room temperature for 1h at a ratio of five Fab
328 fragments per icosahedral asymmetric unit of the virus. A 3μl aliquot of purified
329 HAV full or empty particles or the mixture of full particles and R10 Fab (~1, 0.8 and
330 1 mg/ml respectively) was applied to a freshly glow-discharged 400-mesh holey
331 carbon-coated copper grid (C-flat, CF-2/1-2C, Protochips Inc.). Grids were blotted
332 for 2.5s, in 80% relative humidity for plunge-freezing (Vitrobot; FEI, Hillsboro, OR)
333 in liquid ethane. Cryo-EM data sets were collected at 300kV with an FEI Tecnai G2
334 Polara microscope (FEI, Hillsboro, OR), equipped with a GIF Quantum energy filter
335 (Gatan, Pleasanton, CA) operated in zero-energy-loss mode with a slit width of 20
336 eV, and direct electron detector (K2 Summit; Gatan, Pleasanton, CA). Movies (25
337 frames, each 0.2 s, total dose 25 e⁻ Å⁻²) were recorded with a defocus between 1.2
338 and 2.8 μm in single electron counting mode using SerialEM (35).

339

340 **Image processing, 3D reconstruction, model building and refinement**

341 The frames from each movie were aligned and averaged for the correction of
342 beam-induced drift using MOTIONCORR (36). Particles from micrographs were
343 picked automatically using ETHAN (37) and then manually screened using the boxer
344 program in EMAN (38). The CTF parameters for each micrograph were estimated
345 by using a GPU accelerated program Gctf (39). Cryo-EM structures were determined
346 with Relion 1.3 (40) with the application of icosahedral symmetry. The crystal
347 structure of the HAV full particle (PDB code: 4QPI (7)), low-pass-filtered to 40 Å,
348 was used as an initial model for 3D classification and refinement. For the complex of
349 full particle and Fab, the initial model was created by EMAN2 (41). A total of 4,587
350 HAV full particles, 4,393 empty particles and 1,752 complex particles were used to
351 obtain the final density maps at 3.4 Å, 3.8 Å and 4.2 Å respectively, as evaluated by
352 the so-called “gold standard” Fourier shell correlation procedure between two half
353 maps (threshold = 0.143). The crystal structure of HAV full particle (PDB code:
354 4QPI (7)) was used to fit the HAV full particle, empty particle and complex EM
355 maps. Initial fitting was done manually using the program CHIMERA (42) and then
356 optimized using the “Fit in Map” function in CHIMERA. The fit was further
357 improved with real-space refinement with COOT (28). Fitting of the crystal structure
358 of the R10 Fab molecules was done similarly. All three models were further refined
359 by positional and B-factor refinement in real space using Phenix (16) and rebuilding

in COOT (28) iteratively. The final models were evaluated by Molprobit (43) functions integrated in Phenix. Data and refinement statistics are summarized in Table S1.

Full experimental details are available in *SI Materials and Methods*.

Accession code: The atomic coordinates of HAV empty particle, HAV full particle, NAb R10 Fab and HAV full particle:R10 Fab have been submitted to Protein Data Bank with accession numbers PDB: 5WTF, 5WTE, 5WTG and 5WTH respectively. Cryo-EM density maps of HAV empty, full particle and full particle complexed with R10 Fab have been deposited with the Electron Microscopy Data Bank: EMD-6687 EMD-6686 and EMD-6688 respectively.

Acknowledgements

We thank Jun Dong and Jonathan Diprose for IT support and the OPIC electron microscopy facility and the Center for Biological imaging (CBI), Institute of Biophysics for electron microscopy work. Work was supported by the Ministry of Science and Technology 973 Project (grant nos. 2014CB542800), National Science Foundation grant no. 81330036, no. 31570717 and 81520108019, the Strategic Priority Research Program of the Chinese Academy of Sciences, grant no. XDB08020200 and the MRC grants G100099 and MR/N00065X/1. The work of the Wellcome Trust Centre in Oxford is supported by the Wellcome Trust core award 090532/Z/07/Z. XX Wang was supported by Young Elite scientist sponsorship by CAST. The OPIC electron microscopy facility was founded by a Wellcome Trust JIF

award (060208/Z/00/Z) and is supported by a WT equipment grant (093305/Z/10/Z).

Author Contributions X.W., L.Z., M.D., Z.H, Q.G. Q.T and S.Y. prepared samples, X.W., L.Z., M.D., J.R., Z.H. and T.S.W. assisted in research. X.W., E.E.F, Z.R. and D.I.S. designed the study, all authors analysed data and X.W., L.Z., E.E.F, Z.R. and D.I.S. wrote the manuscript.

References:

1. Drexler JF, *et al.* (2015) Evolutionary origins of hepatitis A virus in small mammals. *Proceedings of the National Academy of Sciences*:201516992.
2. Feng Z, *et al.* (2013) A pathogenic picornavirus acquires an envelope by hijacking cellular membranes. *nature* 496(7445):367-371.
3. Aragonès L, Guix S, Ribes E, Bosch A, & Pintó RM (2010) Fine-tuning translation kinetics selection as the driving force of codon usage bias in the hepatitis A virus capsid. *PLoS Pathog* 6(3):e1000797.
4. Cohen L, Bénichou D, & Martin A (2002) Analysis of deletion mutants indicates that the 2A polypeptide of hepatitis A virus participates in virion morphogenesis. *Journal of virology* 76(15):7495-7505.
5. Tesar M, Jia X-y, Summers DF, & Ehrenfeld E (1993) Analysis of a potential myristoylation site in hepatitis A virus capsid protein VP4. *Virology* 194(2):616-626.
6. Rowlands DJ (2015) Human hepatitis A virus is united with a host of relations. *Proceedings of the National Academy of Sciences*:201520121.
7. Wang X, *et al.* (2014) Hepatitis A virus and the origins of picornaviruses. *nature*.
8. Dang M, *et al.* (2014) Molecular mechanism of SCARB2-mediated attachment and uncoating of EV71. *Protein & cell* 5(9):692-703.
9. Wang X, *et al.* (2012) A sensor-adaptor mechanism for enterovirus uncoating from structures of EV71. *Nature structural & molecular biology* 19(4):424-429.
10. Kaplan G, *et al.* (1996) Identification of a surface glycoprotein on African green monkey kidney cells as a receptor for hepatitis A virus. *The EMBO Journal* 15(16):4282.
11. Yuan S, *et al.* (2015) TIM-1 acts a dual-attachment receptor for Ebolavirus by interacting directly with viral GP and the PS on the viral envelope. *Protein & cell* 6(11):814-824.
12. Lin J, *et al.* (2012) Structure of the Fab-labeled “breathing” state of native poliovirus. *Journal of virology* 86(10):5959-5962.
13. Plevka P, *et al.* (2014) Neutralizing antibodies can initiate genome release from human

- 415 enterovirus 71. *Proceedings of the National Academy of Sciences* 111(6):2134-2139.
- 416 14. Silberstein E, *et al.* (2003) Alteration of hepatitis A virus (HAV) particles by a soluble form of
 417 HAV cellular receptor 1 containing the immunoglobulin-and mucin-like regions. *Journal of*
 418 *virology* 77(16):8765-8774.
- 419 15. Scheres SH & Chen S (2012) Prevention of overfitting in cryo-EM structure determination.
 420 *Nature methods* 9(9):853-854.
- 421 16. Afonine PV, *et al.* (2012) Towards automated crystallographic structure refinement with
 422 phenix. refine. *Acta Crystallographica Section D: Biological Crystallography* 68(4):352-367.
- 423 17. Kuznetsov YG, Daijogo S, Zhou J, Semler BL, & McPherson A (2005) Atomic force microscopy
 424 analysis of icosahedral virus RNA. *Journal of molecular biology* 347(1):41-52.
- 425 18. Gouet P, *et al.* (1999) The highly ordered double-stranded RNA genome of bluetongue virus
 426 revealed by crystallography. *Cell* 97(4):481-490.
- 427 19. Shakeel S, *et al.* (2015) Structural basis of human parechovirus neutralization by human
 428 monoclonal antibodies. *Journal of virology* 89(18):9571-9580.
- 429 20. Ren J, *et al.* (2013) Picornavirus uncoating intermediate captured in atomic detail. *Nature*
 430 *communications* 4.
- 431 21. Springer TA & Wang J-H (2004) The three-dimensional structure of integrins and their
 432 ligands, and conformational regulation of cell adhesion. *Advances in protein chemistry*
 433 68:29-63.
- 434 22. Cavanagh D, Rowlands D, & Brown F (1978) Early events in the interaction between
 435 foot-and-mouth disease virus and primary pig kidney cells. *Journal of general virology*
 436 41(2):255-264.
- 437 23. Kotecha A, *et al.* (2015) Structure-based energetics of protein interfaces guides
 438 foot-and-mouth disease virus vaccine design. *Nature structural & molecular biology*
 439 22(10):788-794.
- 440 24. Walter TS, *et al.* (2005) A procedure for setting up high-throughput nanolitre crystallization
 441 experiments. Crystallization workflow for initial screening, automated storage, imaging and
 442 optimization. *Acta Crystallographica Section D: Biological Crystallography* 61(6):651-657.
- 443 25. Minor W & Otwinowski Z (1997) HKL2000 (Denzo-SMN) Software Package. Processing of
 444 X-ray Diffraction Data Collected in Oscillation Mode. *Methods in Enzymology,*
 445 *Macromolecular Crystallography, Academic Press, New York.*
- 446 26. Hewat EA, *et al.* (1997) Structure of the complex of an Fab fragment of a neutralizing
 447 antibody with foot - and - mouth disease virus: positioning of a highly mobile antigenic
 448 loop. *The EMBO Journal* 16(7):1492-1500.
- 449 27. McCoy AJ, *et al.* (2007) Phaser crystallographic software. *Journal of applied crystallography*
 450 40(4):658-674.
- 451 28. Emsley P & Cowtan K (2004) Coot: model-building tools for molecular graphics. *Acta*
 452 *Crystallographica Section D: Biological Crystallography* 60(12):2126-2132.
- 453 29. Adams PD, *et al.* (2010) PHENIX: a comprehensive Python-based system for macromolecular
 454 structure solution. *Acta Crystallographica Section D: Biological Crystallography*
 455 66(2):213-221.
- 456 30. De Colibus L, *et al.* (2014) More-powerful virus inhibitors from structure-based analysis of

- HEV71 capsid-binding molecules. *Nature structural & molecular biology*.
31. Zhu L, *et al.* (2015) Structure of Ljungan virus provides insight into genome packaging of this picornavirus. *Nature communications* 6.
 32. Walter TS, *et al.* (2012) A plate-based high-throughput assay for virus stability and vaccine formulation. *Journal of virological methods* 185(1):166-170.
 33. Shu P-Y, *et al.* (2003) Development of group-and serotype-specific one-step SYBR green I-based real-time reverse transcription-PCR assay for dengue virus. *Journal of clinical microbiology* 41(6):2408-2416.
 34. Livak KJ & Schmittgen TD (2001) Analysis of relative gene expression data using real-time quantitative PCR and the 2- $\Delta\Delta$ CT method. *methods* 25(4):402-408.
 35. Mastronarde DN (2005) Automated electron microscope tomography using robust prediction of specimen movements. *Journal of structural biology* 152(1):36-51.
 36. Li X, *et al.* (2013) Electron counting and beam-induced motion correction enable near-atomic-resolution single-particle cryo-EM. *Nature methods* 10(6):584-590.
 37. Kivioja T, Ravanti J, Verkhovsky A, Ukkonen E, & Bamford D (2000) Local average intensity-based method for identifying spherical particles in electron micrographs. *Journal of structural biology* 131(2):126-134.
 38. Ludtke SJ, Baldwin PR, & Chiu W (1999) EMAN: semiautomated software for high-resolution single-particle reconstructions. *Journal of structural biology* 128(1):82-97.
 39. Zhang K (2016) Gctf: real-time CTF determination and correction. *Journal of structural biology* 193(1):1-12.
 40. Scheres SH (2012) RELION: implementation of a Bayesian approach to cryo-EM structure determination. *Journal of structural biology* 180(3):519-530.
 41. Tang G, *et al.* (2007) EMAN2: an extensible image processing suite for electron microscopy. *Journal of structural biology* 157(1):38-46.
 42. Pettersen EF, *et al.* (2004) UCSF Chimera—a visualization system for exploratory research and analysis. *Journal of computational chemistry* 25(13):1605-1612.
 43. Chen VB, *et al.* (2010) MolProbity: all-atom structure validation for macromolecular crystallography. *Acta Crystallographica Section D: Biological Crystallography* 66(1):12-21.
 44. Xiao C & Rossmann MG (2007) Interpretation of electron density with stereographic roadmap projections. *Journal of structural biology* 158(2):182-187.
 45. Kucukelbir A, Sigworth FJ, & Tagare HD (2014) Quantifying the local resolution of cryo-EM density maps. *Nature methods* 11(1):63-65.
 46. Ashkenazy H, Erez E, Martz E, Pupko T, & Ben-Tal N (2010) ConSurf 2010: calculating evolutionary conservation in sequence and structure of proteins and nucleic acids. *Nucleic acids research*:gkq399.
 47. Larkin M, *et al.* (2007) Clustal W and Clustal X version 2.0. *Bioinformatics* 23(21):2947-2948.
 48. Gouet P, Courcelle E, & Stuart DI (1999) ESPript: analysis of multiple sequence alignments in PostScript. *Bioinformatics* 15(4):305-308.

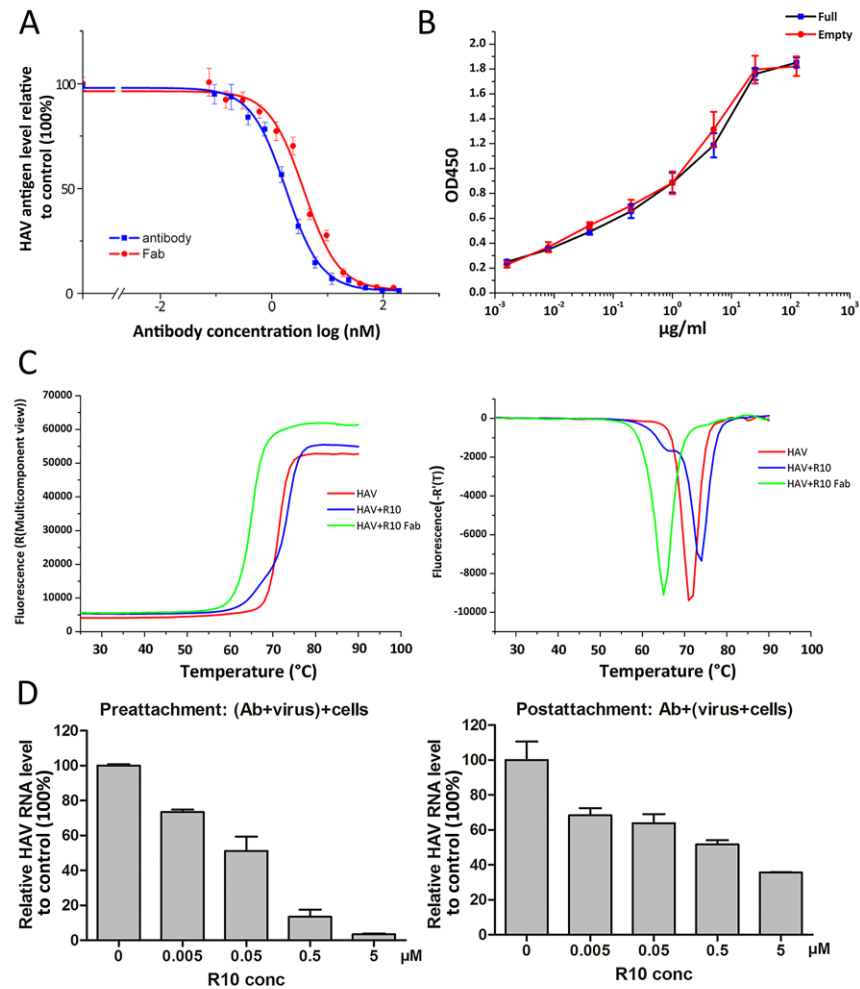


Figure 1 | Characterizations of the monoclonal antibody R10. (A) Neutralization of HAV by R10. Whole Ig G and Fab fragments of R10 were used to block HAV infection at different concentrations by detecting HAV capsids. The red and blue symbols and curves represent whole antibody and Fab fragments respectively. HAV capsids were measured by indirect ELISA and the values are mean from triplicate wells with the standard deviation. (B) Analysis of binding of R10 to HAV mature virions and empty particles by ELISA. 96-well plates were coated with HAV full or empty particles and various concentrations of R10 were added. The amount of bound R10 was detected by HRP assay (Materials and Methods), the parameter on X axis represents the

concentrations of R10, the average OD450 readings from triplicate wells at each dilution with the standard deviation are shown. (C) The stabilities of HAV full particles and their complexes with R10 whole Ig G and Fab fragments at neutral pH were determined by thermofluor assay using the dye SYTO9 to detect RNA exposure (32). The raw fluorescence traces (Left) are shown for HAV full particles (red line) as well as their complexes with R10 whole Ig G (blue line) and Fab fragments (green line) following incubation with SYTO9, whilst their first derivatives are shown (Right). (D) Amount of virus on the cell surface, as detected by RT-PCR, when exposed to R10 before (Left) and after (Right) the virus was allowed to attach to cells. High concentrations of R10 prevent attachment of HAV to the cell surface when HAV is exposed to R10 before cell attachment and R10 can strip HAV off the cell surface when HAV is exposed to R10 post attachment. Values are mean \pm s.d. Experiments were repeated in triplicate.

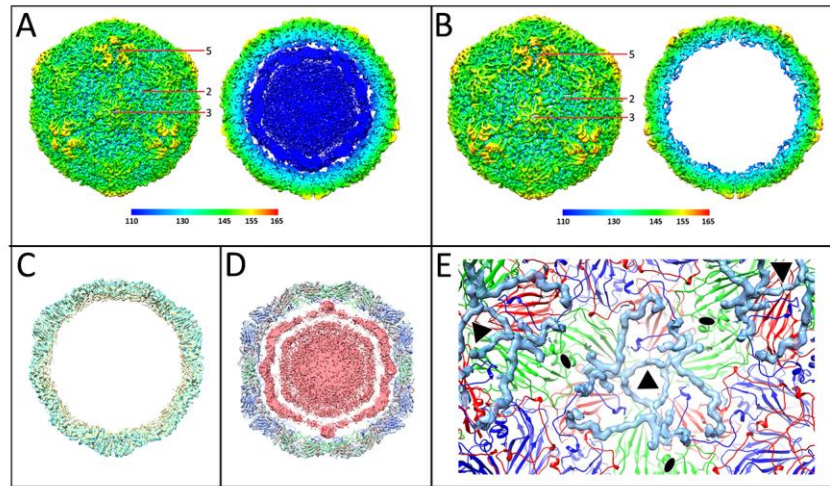


Figure 2 | Structural comparisons of HAV full and empty particles. 3D reconstructions of HAV full particle (**A**) and empty particle (**B**) viewed down a 3-fold axis. The central sections of HAV full and empty particles viewed along a 5-fold axis are shown in the right panel of (**A**) and (**B**) respectively. The surface is colored by radius from blue to red. The icosahedral 5-fold, 3-fold and 2-fold axes are labeled as 5, 3 and 2 respectively. (**C**) Superposition of capsid maps of HAV full (pale yellow) and empty (cyan) particles shows indistinguishable external surfaces. (**D**) ~20 Å thick slabs of the full particle reconstruction viewed along a 2-fold axis, with the coordinates of the HAV full particle structure (shown as a cartoon colored as VP1 blue, VP2 green and VP3 red). The densities corresponding to HAV capsids and genome are colored in gray and salmon respectively. (**E**) HAV viewed from inside. Cyan density derived by subtracting the map of the empty particle (with correct scale) from the map of the full particle shows that the N-termini of VP1 and VP2 are well defined, stabilized by RNA in the full particle.

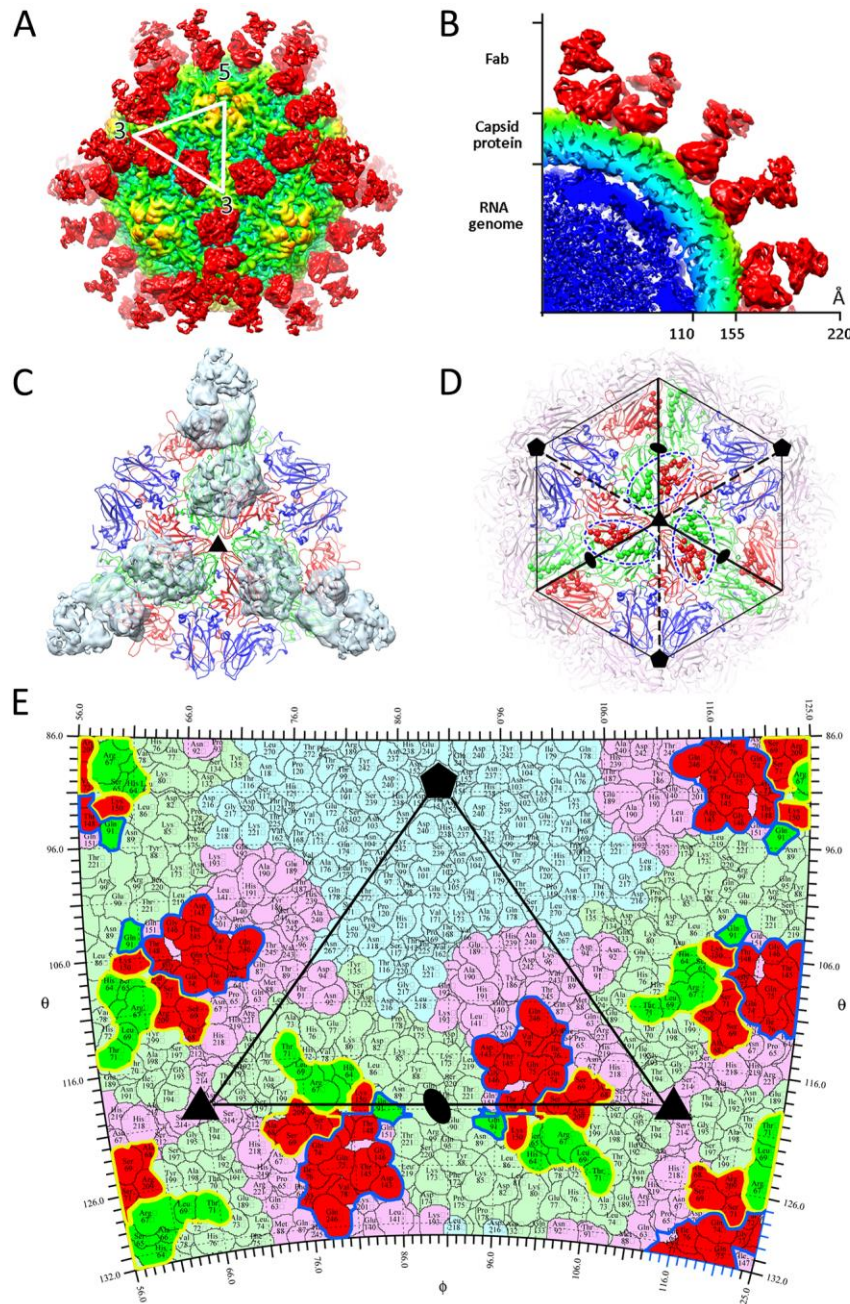


Figure 3 | The 4.2 Å resolution cryo-EM structure of the R10 Fab:HAV full particle complex. (A) Shows the surface and (B) the cross section of the cryo-EM map. One icosahedral asymmetric unit is indicated by a white triangle. (C) The R10 Fab binds to the viral surface along the pentamer interface between the 2-fold and 3-fold axes. (D) The R10 epitopes on six asymmetric units of the HAV surface. VP1, VP2 and VP3 are colored in blue, green and red respectively, residues interacting

with heavy and light chains of the Fab are shown as spheres. The boundary of each epitope is marked with a deep blue dashed ellipse. Positions of 5-, 3- and 2-fold icosahedral symmetry axes are marked as pentagons, triangles and ovals respectively.

(E) The R10 footprints on the HAV surface. The figure shows a 2D projection of the HAV surface produced using RIVEM(44). Residues of VP1, VP2 and VP3 are outlined in pale blue, green and red respectively, residues involved in binding to R10 are shown in brighter colours corresponding to the protein chain they belong to. The footprints of R10 heavy and light chains are indicated by blue and yellow lines respectively. 5-, 3- and 2-fold icosahedral symmetry axes are marked as for **(D)** on one icosahedral asymmetric unit.

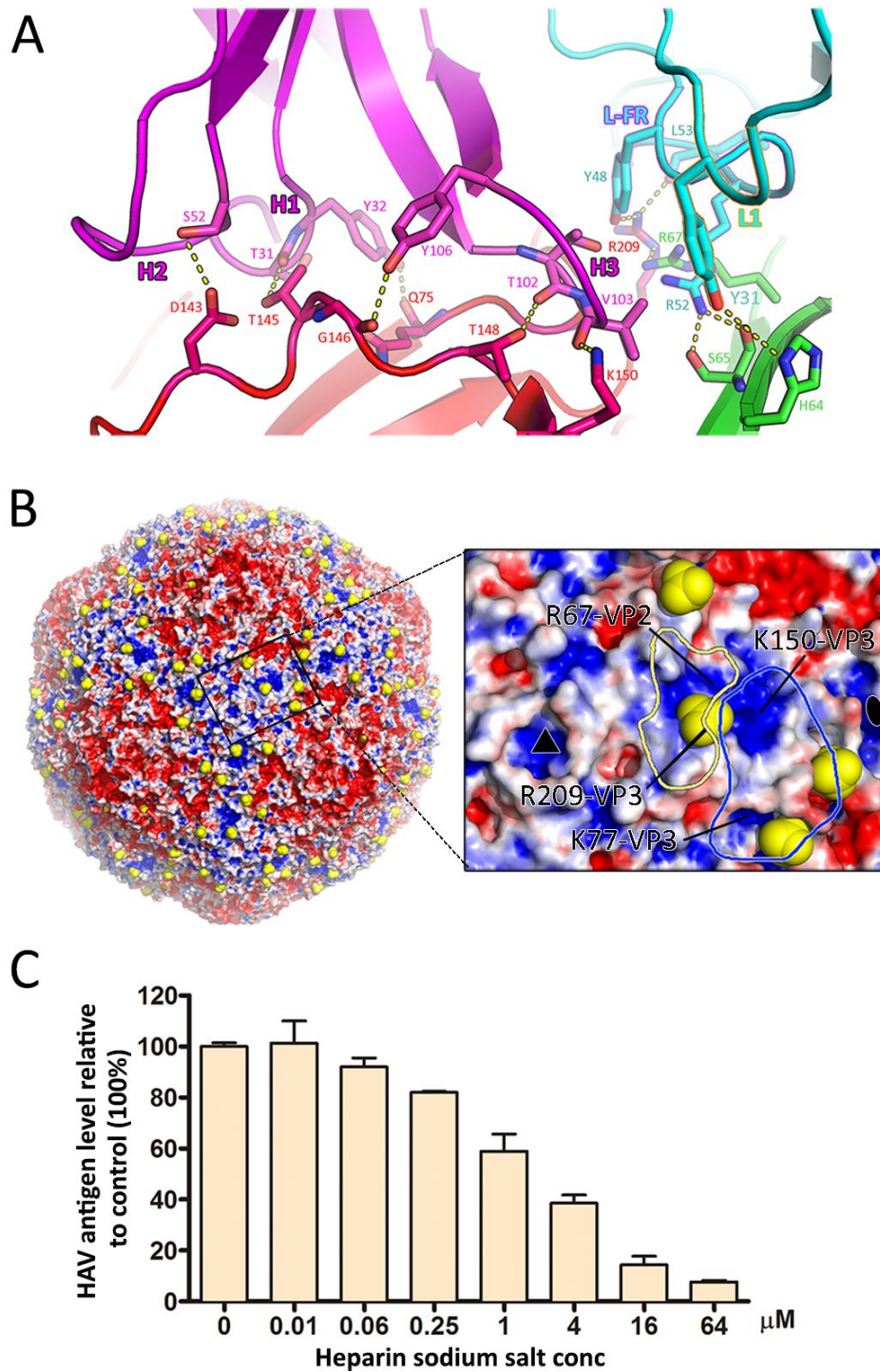


Figure 4 | R10 occupies the positively charged region of HAV surface where glycans on the potential receptors might attach. (A) Interaction between R10 Fab and HAV capsid proteins. Some residues involved in the formation of hydrogen bonds are shown as sticks and labeled. VP2, VP3, light chain and heavy chain are

568 colored in green, red, cyan and magenta respectively. Three CDRs of the heavy chain
569 and epitope on VP2 and VP3 are highlighted by black outlines, The CDR1 and
570 framework region of the light chain are highlighted by orange and purple outlines
571 respectively. **(B)** HAV electrostatic surface (calculated using APBS in PyMOL). Red,
572 blue and white represent negative, positive and no charges respectively. Yellow
573 spheres mark the positions of bound sulphates in the X-ray structure(7). Right panel:
574 Close up. Regions correlated with the R10 heavy and light chains binding sites are
575 indicated by blue and yellow lines respectively. Residues that dominate the
576 positively charged surface, as well as interacting with R10, are labeled. **(C)**
577 Dose-dependent inhibition of HAV infection by heparin sodium. Various
578 concentrations of heparin sodium were preincubated with HAV for 1 h at room
579 temperature before infection of 2BS cells. The inhibitory ability of the sodium salt of
580 heparin was evaluated by determining HAV antigen content using indirect ELISA.
581 Values are mean \pm s.d. Experiments were repeated in triplicate.

582